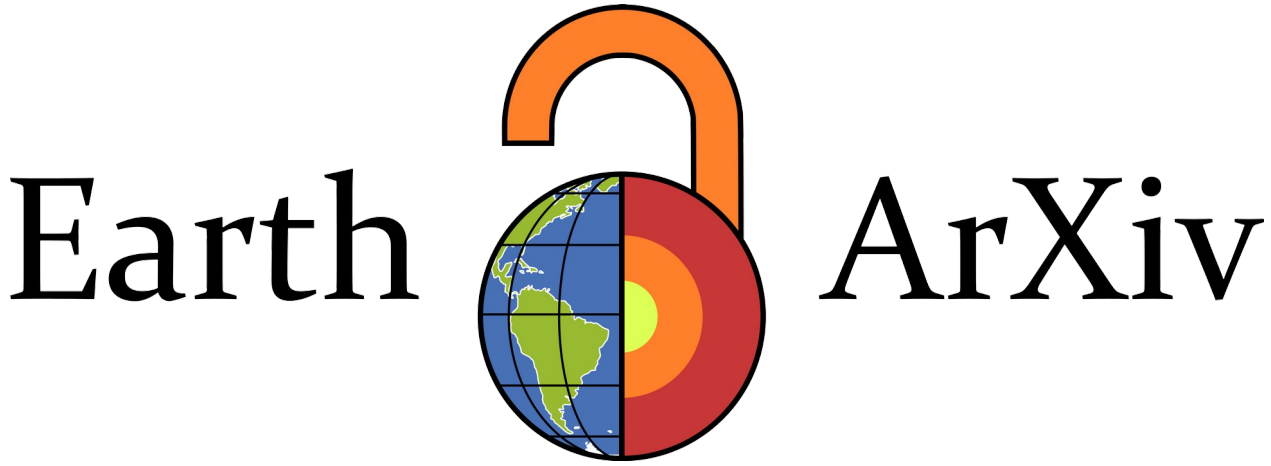

This manuscript has been submitted for publication in **Chemical Geology**. Please note the manuscript has yet to be formally accepted for publication. Subsequent versions of this manuscript may have slightly different content. If accepted, the final version of this manuscript will be available via the 'Peer-reviewed Publication DOI' link on the right-hand side of this webpage. Please feel free to contact any of the authors; we welcome feedback.

Structural and dynamical properties of hydrous magmatic liquids at high pressure: insights from Raman spectroscopy observations during diamond anvil cell experiments.

Lauréna Mourand[1], Clément Ferraina[1,2], Salomé Pannefieu[1], Cyril Aubaud[1], Charles Le Losq[1,3,*]

[1]Université Paris Cité, Institut de physique du globe de Paris, CNRS, Paris, France

[2]Université de Lorraine, CNRS, CRPG, F-54000 Nancy, France

[3]Institut Universitaire de France, Paris, France

*Corresponding author: lelosq@ipgp.fr

Abstract

Silicate liquids play a central role in the differentiation and internal dynamics of terrestrial planets by controlling the transport of heat and matter. One of their key properties is viscosity, which can be strongly influenced by pressure. Currently, there is not enough data to develop general models of viscosity at high pressure. Besides, data on the short and medium range order structure of high-pressure silicate melts are insufficient to draw general structural laws and use them to express the effect of pressure on melt properties. Here we present a new method involving an internally-heated membrane diamond anvil cell coupled with a Raman spectrometer. This setup allowed us to acquire *in situ* Raman spectra of water-bearing sodium aluminosilicate glasses and melts with controlled composition, and to observe how the glass transition temperature, a parameter directly related to melt viscosity, changes with pressure. The results reveal a non-linear behavior of the glass transition temperature with pressure, with a minimum around 6 GPa and a strong increase at higher pressures. The interpretation of undercooled melt Raman spectra shows that this behavior results from a competition between structural compaction, melt polymerization and changes in the coordination of Si, Al network former cations. At pressures above 6-7 GPa, once coordination changes dominate, melts with very different chemical compositions exhibit remarkably similar positive T_g(P) slopes.

Keywords

Silicate melt, glass, high pressure, diamond anvil cell, Raman spectroscopy

1. Introduction

Magma viscosity controls convective dynamics, crystal settling, metal segregation and heat transport in magma oceans (e.g., Solomatov, 2015), which play a key role in planetary differentiation processes (Elkins-Tanton, 2012). In differentiated rocky planets, magma viscosity controls heat and mass transfers in their mantle and crust because it

determines magma mobility. Current data allow building viscosity models that account for the effects of magma composition, temperature, and crystals/bubbles (see for reviews Mader et al., 2013; Russell et al., 2022; Kolzenburg et al., 2022). However, the effect of pressure, significant at mantle scale, is not yet well constrained. Experimental and atomistic simulation data (e.g., Cochain et al., 2017; Xie et al., 2021; Bajgain et al., 2022; Huang et al., 2024) allow building predictive models for a narrow range of melt compositions pertinent to the Earth (e.g., Russell et al., 2024) but are too scarce to constrain general models that could be pertinent to simulate processes on other (exo)planets (Le Losq et al., 2025).

A promising route toward solving this limitation would be to leverage our understanding of the pressure effect on silicate melt structure, in order to develop structure-based predictive models of physical properties such as viscosity and density, as done at ambient pressure (e.g. Mysen, 1995; Doweidar, 1996; Le Losq and Neuville, 2017). Such a structural approach would also improve our understanding of processes that depend on silicate melt structure, such as high pressure metal-silicate partitioning during planetary differentiation (e.g., see Siebert et al., 2011; Huang et al., 2021).

However, the current understanding of the effect of pressure on silicate melt structure is incomplete. Existing experimental and molecular dynamics data document the effect of pressure on the local environment (coordination) of major elements (e.g., see Sakamaki and Ohtani, 2022 for a review). They show a general, smooth densification of silicate melt structure with increasing pressure, with increased coordination of network former (Si, Al) and other (Ca, Mg, Na, K, Fe) cations (Bauchy, 2012; Wang et al., 2014; Drewitt et al., 2015; Sanloup, 2016; Huang et al., 2022; Sakamaki and Ohtani, 2022; Caracas, 2024). However, to propose structure-based models of the effect of pressure on properties such as viscosity, we lack a general description of how pressure affects the 2D/3D arrangement and interactions of cations at medium range order (i.e. a few tetrahedral units), a key knowledge for understanding melt properties as shown by room pressure studies (e.g., Greaves and Ngai, 1995; Greaves and Sen, 2007; Le Losq et al., 2017).

Raman spectroscopy may help solve this issue. This method has shaped our vision of the atomic structure of melts and glasses at ambient pressure (Mysen et al., 1982a; McMillan, 1984; Mysen, 1990; Neuville and Mysen, 1996; Mysen, 1999; Neuville, 2006; Le Losq et al., 2015b, 2017, 2022). It allowed not only to study the connectivity of tetrahedral units at short range order in silicate glasses and melts (e.g. Mysen et al., 1982b; McMillan, 1984; Mysen, 1990; Mysen and Frantz, 1993; Mysen, 1999; Neuville, 2006; Le Losq et al., 2015b), but also how changes at the medium range order (2D/3D tetrahedral organisation in rings and cages, clustering/channeling of metal cations, high/low density regions, etc, see e.g. Greaves and Sen, 2007) are related to melt composition and affect their dynamic and thermodynamic properties (e.g. Neuville and Mysen, 1996; Le Losq and Neuville, 2013, 2017; Pannefieu et al., 2024). At high pressure, Raman studies have demonstrated that glass densification results from pressure-induced reductions in intertetrahedral T-O-T angles (T = Si, Al), increases in Si and Al coordination, changes in ring/cage statistics, and progressive polymerization in a variety of silicate glasses (e.g. Hemley et al., 1986; Wolf et al., 1990a; Moulton et al., 2016; Muniz et al., 2016; Weigel et al., 2016; Moulton et al., 2019; Saha et al., 2026). Those

pressure-induced structural changes, observed in glasses, seem related to important variations in melt properties, including viscosity, as revealed by molecular dynamics studies (e.g. Wang et al., 2014; Bajgain et al., 2022; Caracas, 2024). However, we currently lack direct Raman data regarding the structure of aluminosilicate melts at high pressure, in particular above 10 GPa. Such data could allow a joint determination of the effect of pressure on the structure and dynamic properties of silicate melts, which would largely benefit our understanding of aluminosilicate melt behaviour at pressures relevant to the upper mantle.

In this publication, we present Raman data acquired *in situ* at high pressure and high temperature, on a water-bearing sodium aluminosilicate glass and undercooled melt. The experiments aimed at documenting, via Raman spectroscopy, how the glass/melt atomic structure changes with pressure, and how this relates to variations in a dynamic property directly linked to melt viscosity: the glass transition temperature T_g. To perform those experiments, we used a membrane diamond anvil cell (MDAC) equipped with an internal resistive furnace. This setup allows currently reaching temperatures of 800 °C, and pressures of 20 GPa with 400 micrometer culet diamonds. Working at stable high temperatures in DAC setups is always challenging, so to limit any issue, we focused on a composition with very low glass transition and liquidus temperatures: the Albite-Nepheline-$Na_2Si_4O_9$ eutectic, hereafter abbreviated ANN, to which we added 5 wt% water in order to reduce as much as possible working temperatures. Another advantage of this composition is that sodium aluminosilicate glasses have been extensively studied using Raman spectroscopy at room pressure (e.g. Mysen, 1990; Mysen et al., 2003; Mysen, 2007; Le Losq et al., 2014, 2015b), making the interpretation of their Raman spectra straightforward, at least at room pressure. Raman spectra of the hydrous glasses and melts were acquired at pressures up to 13 GPa, and temperatures up to 500 °C. T_g were estimated using the disappearance of deviatoric stress in a MDAC (Piermarini et al., 1973; Ribeiro et al., 2014a; Ransom and Oliver, 2017). The obtained dataset documents the structural and dynamic (T_g) evolution of the water-bearing ANN glass/melt as a function of temperature and pressure.

2. Experimental Methods

The selected water-free ANN composition eutectic temperature is 732 ± 5 °C (Schairer and Bowen, 1956). The 1-atm T_g of the ANN glass is 501 ± 12 °C (calculated with i-Melt, Le Losq and Baldoni, 2023). We added 5 wt% water into the glass using a piston-cylinder apparatus, such that the estimated T_g is 277 ± 56 °C using the model of Debeuner et al. (2003). The following sections describe the synthesis of the starting glass material, the preparation and characterization of the hydrous glass, and the realization of the MDAC experiments.

2.1. Glass synthesis

To prepare the volatile-free starting glass compositions, a mixture of reagent grade Na_2CO_3 (dried overnight at 350 °C), Al_2O_3 and SiO_2 (dried overnight at 1000 °C) oxide powders was prepared by weighing the different oxides and mixing/crushing them in an agate

mortar. The mixture was then placed in a Pt crucible and a first decarbonation step was performed in a muffle furnace, followed by full melting in a vertical tube furnace at 1300 °C. Quenching the melt allows obtaining a glass that was crushed and melted again. In total, three cycles of grinding, melting and quenching were performed to obtain homogeneous starting glass materials. The composition of the starting glass was checked with a Jeol JXA-iHP200F EMPA at the CAMPARIS Paris VI service, with a 4 nA beam defocused to 20 micrometres. In wt%, the nominal ANN composition is 61.5 SiO_2, 12.5 Al_2O_3, 26.0 Na_2O, and the measured ANN composition was 59.9(5) SiO_2, 12.7(5) Al_2O_3, 26.6(3) Na_2O, 0.1(1) MgO+CaO+FeO+K_2O, summing to 99.3(7).

2.2. Piston-Cylinder experiments

To prepare hydrous ANN glasses from melts at high temperature and pressure, the starting materials were contained in ≈10 mm long, ≈5 mm diameter platinum capsules. The appropriate amount of water was added first (from ≈1 to ≈12 µL) with a microsyringe (precision ±0.1 µL). The exact amount of water was determined by weighing the capsule after addition of water. The crushed, anhydrous silicate glass was then added (typically 130 to 150 $\times 10^{-3}$ g) and the capsules were welded shut. A final weighing step was performed to check if capsules were perfectly sealed by weighing them before and after heating to 300 °C for 1 h. This step also allows an homogeneous distribution of the water in the capsule. The samples were then placed in 3⁄4″-diameter talc-pyrex furnace assemblies from Ceramic Substrates and subjected to a pressure of 1.2 GPa and a temperature of 1400 °C for 120 min in a solid-medium, high-pressure Voggenreiter Mavo press LPC 250 - 300/50 apparatus available at IPGP. Temperatures were measured with a type C thermocouple. Pressure was calibrated against the quartz-coesite transition, following the steps described in Condamine et al. (2022), to determine the friction coefficient of our press. Estimated uncertainties are ~10 °C and ~0.1 GPa, respectively.

2.3. Infrared spectroscopy

The obtained hydrous glass were analyzed by Fourier-Transform InfraRed (FTIR) spectroscopy at IPGP with a Spectra Tech IR Plan infrared microscope combined to a Thermo Scientific Nicolet 6700 spectrometer, with a Ge-KBr separator, an Everglow source operating at 1140 °C and a MCT-A detector covering a frequency range from 600 to 11,700 cm^{-1}. Samples were initially double-polished using ethanol at a thickness of around 300-400 µm. Transmission spectra were recorded with a ×10 objective and a 100 µm field of view, a spectral resolution of 4 cm^{-1}, and performing 300 scans per spectrum.

To determine the glass water content from the FTIR spectra, we followed the following data treatment procedure. First, a third-order polynomial baseline was employed for subtracting the background in the frequency range of interest (4000–5800 cm^{-1}). Then, we measured the integrated areas beneath the ≈4500 and ≈5200 cm^{-1} absorption bands, assigned to vibrations of hydroxyl groups OH^- and molecular water H_2O_{mol} species, respectively

(Stolper, 1982; Silver et al., 1990; Yamashita et al., 2008; Le Losq et al., 2015a). To calculate the concentrations of OH^- and H_2O_{mol} from the measured integrated areas, integrated absorption coefficients are required. The anhydrous ANN glass has a Non-Bridging Oxygen to Tetrahedral unit ratio (NBO/T) of 0.47, slightly lower than that of sodium tetrasilicate glass (0.5). Therefore, given these structural similarities, we used integrated absorption coefficient values available for sodium tetrasilicate glass, of 102 and 114 L mol^{-1} cm^{-2} for OH^- and molecular water H_2O_{mol}, respectively (Yamashita et al., 2008).

Using those integrated absorption coefficient values, we found a concentration of 1.28(8) wt% of hydroxyl OH^- groups, and 3.89(16) wt% of molecular water H_2O_{mol}. The total water concentration of the starting hydrous glass material is thus equal to 5.17(18) wt%, a value that compares very well with a nominal concentration of 5 wt%.

2.4. Diamond Anvil Cell experiments

We used a MDAC apparatus from the BETSA company, equipped with Boehler-Almax diamonds with culet sizes of 400 micrometers, and ZrO_2 seats. Pressure was controlled via a gas membrane. High temperatures were achieved using an internal heating system composed of Kanthal elements that heat the gasket. The theoretical limit of the heating elements is 1400 °C, and we reached 750 °C with this setup during tests. Routine use in the 200-600 °C range is straightforward, which is ideal as this range encompasses the T_g of the ANN glass containing 5 wt% H_2O. Temperature was measured via a type K thermocouple glued on the lower anvil, as close as possible from the diamond tip but making sure that it did not touch the gasket. Uncertainty on temperature with this setup is evaluated to be ± 10 °C (1σ) for T below 500 °C, following Hwang et al. (2023). Rhenium gaskets of an initial thickness of approximately 200 micrometers were used. They were pre-indented to a thickness of approximately 60-70 micrometers. A sample hole of 190 micrometers diameter was drilled into the gasket using an in-house picosecond laser cutting system available at IPGP. The same system was used to prepare ANN + 5 wt% glass cylinders of 180 µm diameter by 60 µm thickness (Figure 1). The cylinders were checked for any water loss as a result of the laser cutting process: no variation of the 3600 cm^{-1} O-H stretching Raman signal was observed on the prepared samples, confirming the absence of any significant water loss, at least a few micrometers away from the borders of the sample.

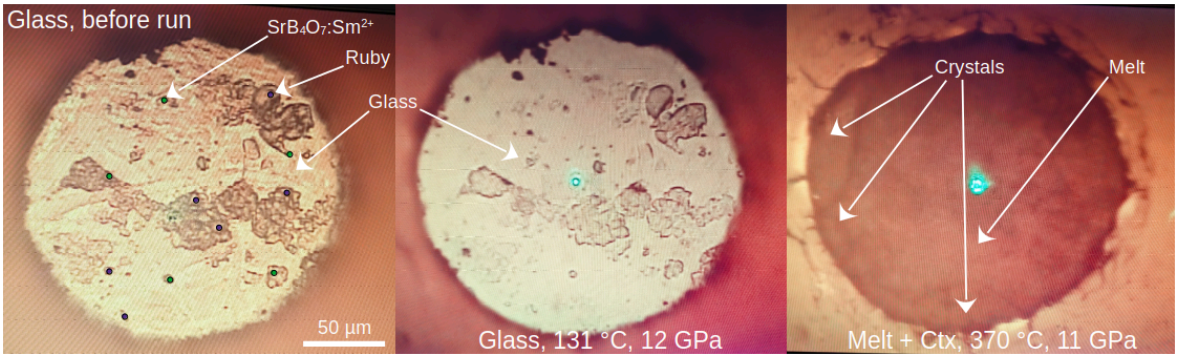

Figure 1: Images from one MDAC experiment with the ANN + 5 wt% H_2O composition. Left: the experiment starts with a glass cylinder that fills the Re gasket hole; on top of the glass, we observe pieces of broken rubies and $SrB_4O_7:Sm^{2+}$ pressure sensors, whose fluorescence signals were measured on the red and green spots, respectively. Middle: image of the sample chamber at 12 GPa with glass material at 131 °C. Right: image of the melt that is undergoing slow crystallization at 11 GPa and 370 °C; the sample appears darker as the back diamond broke at 350 °C, preventing proper light transmission.

The glass cylinders were then loaded in Re gaskets together with pieces of ruby and $SrB_4O_7:Sm^{2+}$ pressure sensors (Datchi et al., 2007; Shen et al., 2020). Ruby has a fluorescence band near 490 nm sensitive to pressure and temperature, and that of $SrB_4O_7:Sm^{2+}$ near 485 nm is mostly sensitive to pressure. The different pressure sensors allowed measuring the pressure in the cell, as well as the pressure gradients. The aim was to leverage the diminution of deviatoric stresses in the DAC as the glass transition was crossed when heating a glass slowly toward high temperature. Indeed, crossing the T_g results in an homogenization of the parameters (peak position, peak width…) of the spectra collected on different pressure sensors, marking the decrease in the deviatoric stresses in the DAC as the undercooled liquid starts to redistribute the stress. This method has been used on different liquids such as cumene, showing interesting results (Ribeiro et al., 2014a; Ransom and Oliver, 2017). For the present experiments, after an initial compression of the sample at room temperature, pressure was set to the desired value and temperature was increased slowly. We then made dwells at the desired temperature: at each dwell, we waited 10 minutes for sample relaxation and then recorded the fluorescence spectra of the different pressure markers and the Raman spectra of the glass/melt, using an Andor Shamrock 500i-A spectrometer coupled to a Andor CCD DU401A-BV detector and a Ventus 532 nm laser excitation line. The experiments were continued until triggering crystallization of the undercooled melt above T_g, in order to confirm that we indeed crossed the T_g and had a melt in the cell. This was performed for all experiments. We attempted to analyse the materials after the experiments during the EMPA session, but they underwent substantial crystallization at high temperature accompanied by volatile saturation of the melt and water exsolution in fluid pockets. Upon decompression and opening of the DAC, the fluid/crystal/glass mixtures changed significantly, forming a modified, crystal- and porous-rich (due to the loss of fluids) material in the gasket that quickly reacted with the atmosphere. As a result, analysing the material after the experiments, outside the DAC, did not yield interesting results.

Six runs were successfully performed (Fig. 2). After acquisition, fluorescence and Raman spectra were treated using the Rampy library (Le Losq, 2018) in Python. For the Ruby fluorescence R1 line, we determined its position after subtracting a linear background and slightly smoothing the spectra using a Whittaker smoother. Pressure was then calculated using the IPPS-Ruby2020 pressure gauge (Shen et al., 2020), with temperature correction from Datchi (2007). For the $SrB_4O_7:Sm^{2+}$ pressure sensor, we performed a similar treatment to get the position of the $^5D_0 - ^7F_0$ fluorescence line and then used the equations from Datchi (2007). The 400-1250 cm^{-1} portion of Raman spectra of glasses and melts contained a

diamond background, which was recorded during the experiments with the same laser focus and conditions as the sample Raman spectra, but on the gasket. The obtained background was adjusted in intensity and then removed (Dalou et al., 2015; Le Losq et al., 2022), allowing us to recover diamond-free glass/melt Raman spectra in the 400-1250 cm^{-1} Raman shift range. No background was removed for signals acquired at higher Raman shifts, including from O-H stretching at around 3500 cm^{-1}. After background removal, the 400-1250 cm^{-1} portion of Raman spectra of samples was corrected from temperature and excitation line effects using the so-called "Long" correction (Shuker and Gammon, 1970; Galeener and Sen, 1978; Brooker et al., 1988; Le Losq et al., 2014), and intensity was normalised to the area under the curve.

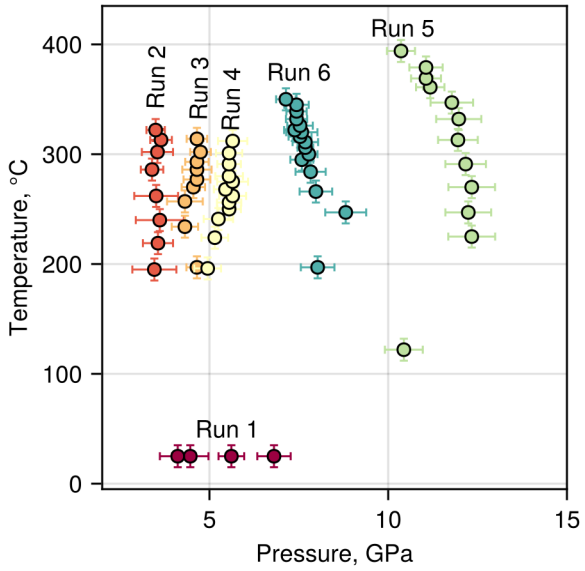

***Figure 2**: Pressure - temperature paths of the six successful runs that were performed. Here, we report the mean pressures (and their associated standard deviations) calculated from the $^5D_0 - ^7F_0$ line of several grains of $SrB_4O_7:Sm^{2+}$ dispersed in the sample chamber (see Fig. 1).*

The background-corrected 400-1250 cm^{-1} portion of Raman signals was further analysed using two methods: (i) principal component analysis (PCA) of the 400-800 cm^{-1} portion of the signal, and (ii) peak fitting the 800-1250 cm^{-1} portion of the signals. The 400-800 cm^{-1} portion of the Raman signal of glasses and melts record inter-tetrahedral vibrations of the aluminosilicate network (e.g., McMillan, 1984). It is particularly suited to track changes in inter-tetrahedral angle and bonding upon increasing pressure (Hemley et al., 1986; Wolf et al., 1990b; Weigel et al., 2016; Moulton et al., 2019). To have a reduced vision of its changes with pressure, we performed a PCA of this portion of the Raman signal for all runs, looking at the main 3 components that account for ≈ 90 % of the variance of the data. We also calculated the centroid of the 400-800 cm^{-1} portion of the Raman signals, which

usually increases significantly with increasing pressure because of a decrease in inter-tetrahedral angle (e.g., Weigel et al., 2016).

A broad band is visible in the 800-1250 cm^{-1} portion of the silicate glass/melt Raman spectra: it is assigned to intra-tetrahedral (Si,Al)-O stretching vibrations in the tetrahedral Q^n units, with n the number of bridging oxygens they carry (e.g., see Virgo et al., 1980; Mysen et al., 1982a; McMillan, 1984; Mysen et al., 2003; Le Losq et al., 2014, 2022). We decomposed it using five bands (for details on assignments, see Le Losq et al., 2015b, 2022 and references cited therein): a Gaussian peak near 900 cm^{-1} assigned to vibrations of T-OH groups with T = Si, Al (Stolper, 1982; Malfait, 2009; Le Losq et al., 2015b), a Gaussian peak near 960 cm^{-1} assigned to Si-O stretching in Q^2 units (Brawer and White, 1977, 1975; Furukawa et al., 1981; Mysen et al., 1982a), a Gaussian peak near 1030 cm^{-1} whose assignment is debated and discussed below, a pseudo voigt peak near 1070 cm^{-1} assigned to T-O stretching in Q^3 units (Brawer and White, 1977, 1975; Furukawa et al., 1981; Mysen et al., 1982a; Nesbitt et al., 2019), and a Gaussian peak near 1130 cm^{-1} assigned to T-O stretching in Q^4 units (Brawer and White, 1977, 1975; Furukawa et al., 1981; Mysen et al., 1982a; Le Losq et al., 2014). See Supp. Fig. 1 for examples of fits on two Raman spectra of undercooled melts at around 3 and 12 GPa.

While assignments of the TOH, Q^2, Q^3 and Q^4 peaks are unambiguous, that of T_{2S} is not. This peak has been assigned to asymmetric stretching (T_{2s} mode) of any Q^n units (Le Losq and Neuville, 2013; Spiekermann et al., 2012), to Si-BO stretching in any Q^n unit with BO a Bridging Oxygen (Mysen et al., 1982a), and to an additional low-frequency Q^3 A_1 symmetric stretching mode (Nesbitt et al., 2019; O'Shaughnessy et al., 2020; Nesbitt et al., 2021). In the last proposition, the low-frequency tail of the Q^3 peak is proposed to result from a weakening of Si-O force constants by interactions between metal cations and bridging oxygens (O'Shaughnessy et al., 2020). However, this explanation does not explain the depolarization ratio of this band, its presence in the Raman spectra of fully polymerized glasses such as albite, or a clear 1020-1060 cm^{-1} signal retrieved using multivariate curve resolution on Raman spectra of silicate glasses (see discussion in Le Losq et al., 2022 and references cited therein). This led Le Losq et al. (2022) to assign this band to T–O asymmetric stretching in any Q^n units (T_{2s} vibrational mode) in Raman spectra of water-bearing calcium aluminosilicate glasses. Here, such an assignment is consistent with the fact that the frequency of this peak barely increases with pressure whereas those of the Q^3 and Q^4 peaks significantly increase (Supp. Fig. 2).

We finally caution the reader that all the above peak assignments were made assuming Si and Al in tetrahedral coordination in glasses at room pressure. At high pressure, and particularly above 6-7 GPa, significant fractions of Si and Al may be in five- and six-fold coordination in the glass/melt network (e.g., Wang et al., 2014), altering the validity of the traditional peak fitting approach.

To perform the peak fitting, we used the quasi-Newton algorithm from Tarantola (2005) for adjusting the parameters of the peaks to fit the spectra via gradient descent

ponderated least-square regression. The method is implemented in the Spectra.jl software in the Julia language (Le Losq, 2016).

3. Results

3.1. Glass/melt Raman spectra

The 400-1250 cm^{-1} and 3200-3850 cm^{-1} portions of the sample Raman spectra recorded during the experiments show distinct evolution of the signals as a function of temperature and pressure (Fig. 3). For time constraints, we checked the Raman signal between 1250 and 3200 cm^{-1}, but we did not record it systematically as it was too time consuming. We focused on the two spectral windows visible in Figure 3 because we were able to record them with fixed detector positions. Figure 4 shows comparisons of glass and melt Raman spectra at ambient and high pressures.

The 400-800 cm^{-1} portion of the starting glass Raman spectrum (Fig. 4, bottom) shows two broad bands near 540 and 600 cm^{-1}. Their frequencies shift to higher values upon glass compression, reaching respectively ≈ 560 and 635 cm^{-1} at 5 GPa (Fig. 4). The ≈ 560 cm^{-1} band disappears in the Raman spectra of high temperature glasses and melts (Figs. 3, 4). At 5 GPa and temperatures above 150 °C, only one band at ≈ 650 cm^{-1} is visible. A shoulder near 730 cm^{-1} appears above 10 GPa, and a sharp peak at this frequency further appears upon crystallization at the highest temperatures (Fig. 3).

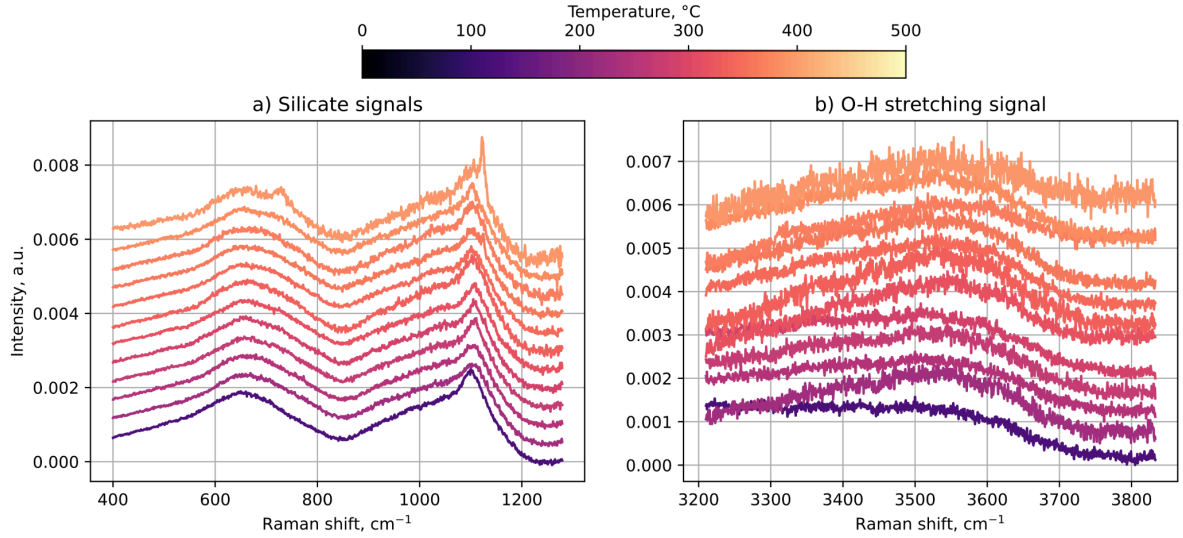

***Figure 3**: (a) Silicate and (b) O-H stretching Raman signals recorded during the run 5 at P ≈ 11-12 GPa (see Fig. 2). Sharp peaks near 730 and 1130 cm^{-1} on the spectra at the highest temperatures are from crystals that nucleated and grew at the end of this experiment (see Fig. 1 for corresponding visual observations).*

In the 800-1250 cm^{-1} portion of the Raman spectra, we observe a broad band. The position of its maximum in intensity shifts to higher values with increasing pressure, from ≈ 1070 cm^{-1} in the Raman spectrum of the starting glass to 1085 cm^{-1} in the Raman spectra of the melt and quenched glass at 5 GPa and high temperatures (Fig. 4). Further comparing the

Raman spectra of the melt and quenched glass at 5 GPa reveals that the differences as a function of temperature are much less visible (Fig. 4): we mostly observed a higher intensity of the shoulder near 1130 cm^{-1}.

The 3200-3850 cm^{-1} portion of the Raman spectra show a broad band typical of water-bearing glass and melts (Fig. 3). The acquisition of this signal was challenging. It showed important variations of its background and signal-to-noise ratio as a function of pressure and temperature. Besides, the current setup allowed us only to record a fraction of the O-H stretching signal, which can extend well below 3200 cm^{-1}. We thus show it in Figure 3 for documentation but did not analyse it further.

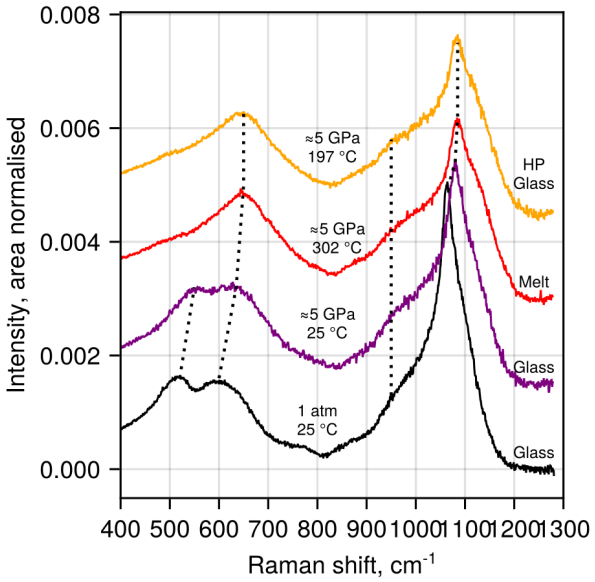

***Figure 4**: Comparison of the 400-1250 cm^{-1} portions of Raman spectra of the starting glass, of a cold-compressed glass at 5 GPa and 25 °C, of a melt at the same pressure but 302 °C, and of a glass quenched from this melt but kept at high pressure and 197 °C.*

Raman signals from crystals appearing in the melts at the highest temperatures (e.g., Fig. 2) materialized by peaks near 695 and 1090 cm^{-1} below 6 GPa (Supp. Fig. 3). At ≈ 10.6 GPa during run 5, we acquired Raman spectra on the crystals at the highest temperature (394 °C, Supp. Fig. 3). They showed sharp peaks near 392, 447, 670, 720, 992, 1032 and 1118 cm^{-1}. Based on Fleet and Henderson (1997), we assign those signals to various high-pressure sodium silicate phases that crystallized from the melts.

3.2. Glass transition temperature determination

Increasing temperature and crossing T_g was marked by changes in the behavior of the pressure sensors weaker than those observed by Ribeiro et al. (2014b) or Ransom and Oliver (2017). We observed subtle decreases in the error bars representing the dispersion of pressure calculated from different pieces of pressure markers, marking (as expected) a decrease of the deviatoric stresses in the sample chamber, and/or changes in the pressure versus temperature

327 trends (Fig. 5a,b). Crossing the T_g also resulted in changes in the evolution of the glass/melt
328 Raman spectra principal components with temperature, e.g. sudden decrease or increase of
329 the principal components, and/or changes in the slopes their values form when reported
330 against temperature (Fig. 5c).

331 For instance, during run 2, we observed a change in the behavior of the pressure
332 determined from the ruby R1 fluorescence line between ≈ 262 and ≈ 286 °C (Fig. 5a) : the
333 pressure versus temperature trend changes slightly, and error bars on pressure are slightly
334 lower above ≈ 262 °C. For $SrB_4O_7:Sm^{2+}$, the error bar on pressure decreased above ≈ 262 °C
335 (Fig. 5b). Those observations indicate a decreasing pressure gradient in the DAC sample
336 chamber above ≈ 262 °C, which we assign to the presence of an undercooled melt
337 redistributing stress. This is corroborated by changes in the temperature behavior of the
338 principal components that describe the 400-800 cm^{-1} portion of the glass/melt Raman spectra
339 (Fig. 5c). When the undercooled melt crystallised at ≈ 313 °C (visual observation), further
340 changes were observed, such as larger error bars on pressure and sharp variations of the
341 principal components (Fig. 5). This is explained by the apparition of a solid in the DAC
342 sample chamber that may participate in increasing deviatoric stress in the sample chamber, as
343 well as in changing the residual melt composition.

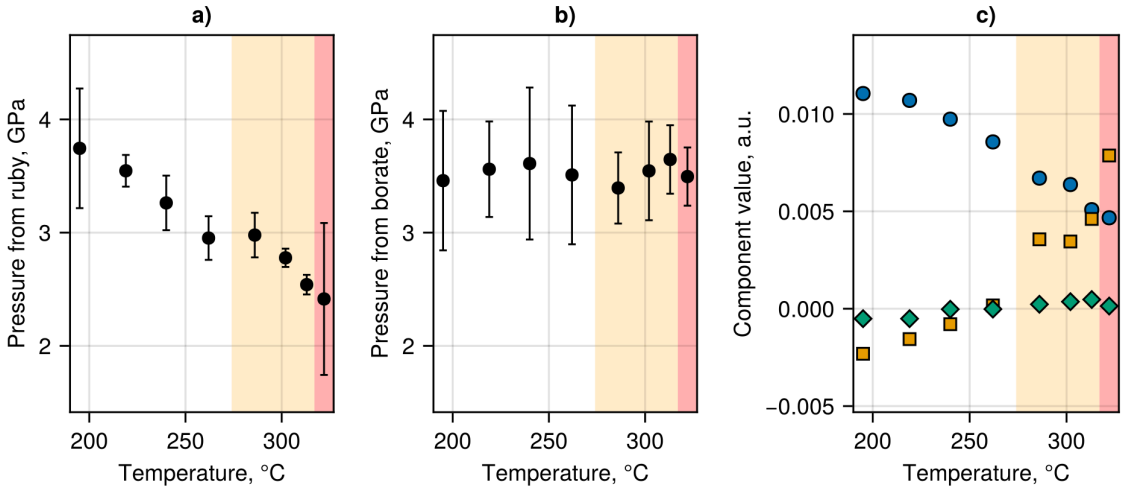

***Figure 5**: Pressure from the ruby (a) and borate (b) sensors during the run 2, and values of the first 3 principal components from the PCA analysis of the 400-830 cm^{-1} portion of glass/melt Raman spectra (c). Error bars on the pressure values are the standard deviation of values from several pressure sensors dispersed in the experimental chamber (Fig. 1); lower error bars indicate a decrease in the pressure gradients within the experimental chamber. Orange regions: temperature domain in which melt was present. Red regions: temperature domain in which crystals were visually observed.*

344 We detected T_g for all of the runs (Fig. 6) by tracking the joint variations in the values
345 of, and/or trends formed by the pressure sensors and the glass/melt Raman spectra principal
346 components (Fig. 5). The T_g of the hydrous glass at ambient pressure is ≈ 277 °C (section 2).
347 Between 0 and 6 GPa, T_g slightly decreases down to a value near 260 °C. At higher pressures,

T_g increases to reach a value between ≈ 332 and ≈ 347 °C at ≈ 12 GPa (Fig. 6). We also observe that the temperature at which undercooled melt crystallization starts increases with pressure. It evolves in parallel with the T_g (Fig. 6, Supp. Fig. 4), as expected from the theory of nucleation (Neuville et al., 2017). Overall, those data indicate a slight decrease of the melt T_g as pressure increases up to 6 GPa, followed by an important T_g increase with increasing further the pressure.

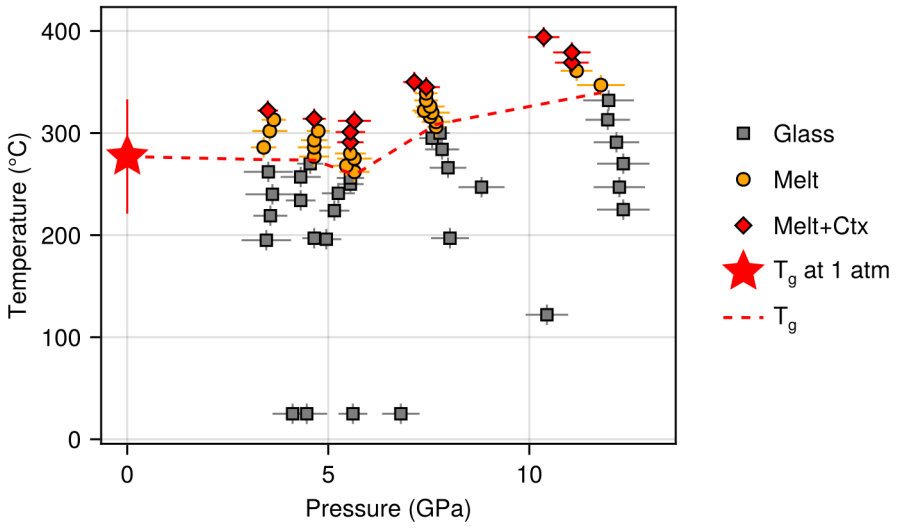

***Figure 6**: Temperature and pressure diagram representing all the data points, as well as the inferred state of the material in the DAC sample chamber. As in Fig. 2, we use here the pressure values derived from the analysis of the $^5D_0$ $-^7F_0$ lines of SrB_4O_7:Sm^{2+}. Ctx: Crystals.*

3.3. Glass/melt polymerization

The analysis of the 830-1250 cm^{-1} portion of the Raman spectra reveals changes in the areas of the different peaks assigned to different Q^n units (Fig. 7, see also Supp. Fig. 1). At a given temperature, the Q^4 peak area decreases with increasing pressure, while that of T_{2S} increases (Fig. 7). With increasing temperature, we observe changes in Q^n area pressure trends upon crossing the T_g. In particular, there is a small but systematic decrease in the Q^3 peak area, which then increases with further increasing temperature in the melt domain (Fig. 7b,c,d,e). Those observations corroborate the glass/melt assignments previously presented (Figs. 5,6).

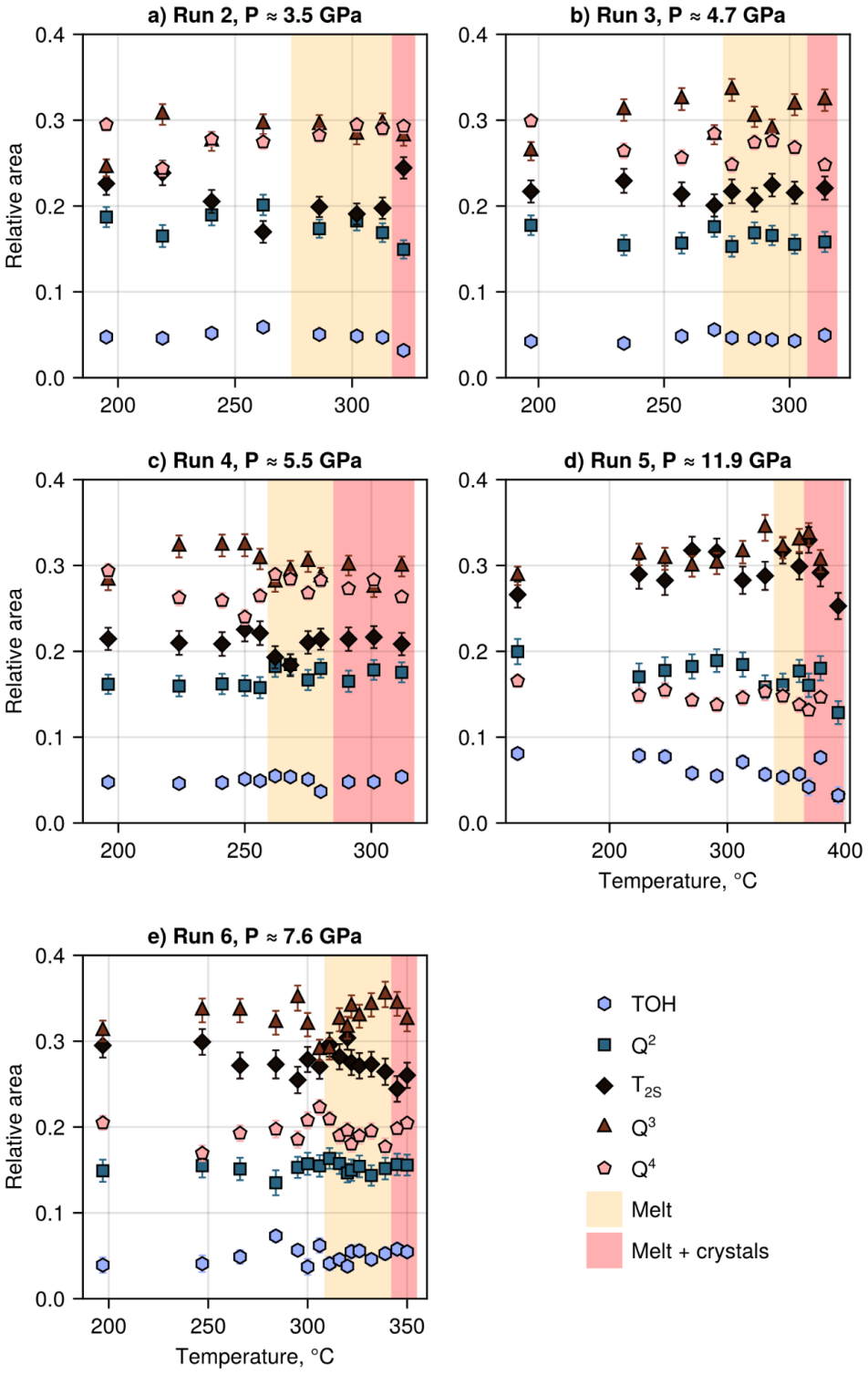

Figure 7: Areas of the different peaks assigned to Raman stretching signals from different tetrahedral units in the glass/melt. See Supp. Fig. 1 for an example of the peak fitting model.

We analysed further the data for non-crystallized high pressure melts (Fig. 8). The frequencies of the Q^3 and Q^4 peaks slightly increase with increasing pressure, while those of the other peaks seem rather constant (Supp. Fig. 2). The areas of all peaks are nearly constant between 2 and 6 GPa (Fig. 8a). Above ~6 GPa, we observe a sharp decrease of the Q^4 peak area, and a sharp increase of that of T_{2S}. The Q^2 and TOH peak areas do not vary significantly with pressure, and that of Q^3 slightly increases above ~6 GPa. The Q^2/Q^3 peak area ratio, a robust marker of melt polymerization (Mysen and Frantz, 1993, 1994), decreases from ~0.6 below 6 GPa down to ~0.5 above this pressure (Fig. 8b). This indicates a slight increase in melt polymerization above 6 GPa.

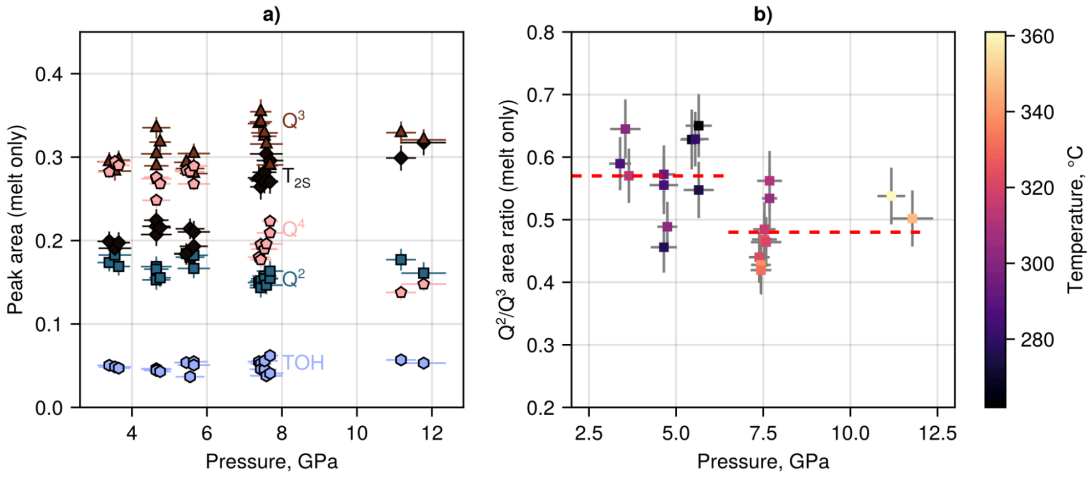

Figure 8: Pressure dependence of (a) the areas of the individual peaks used in the peak fitting modelling of crystal-free melt Raman spectra (all temperatures, see Fig. 6 for melt P-T points), and (b) the Q^2/Q^3 peak area ratios. In (b), the dashed red lines represent the median values of the Q^2/Q^3 ratio before and after 6 GPa.

4. Discussion

Coupling Raman spectroscopy with resistive-heating membrane diamond anvil cell experiments allowed the joint determination of the structural and dynamic properties of water-bearing eutectic albite-nepheline-sodium disilicate ANN glasses and melts at high pressure, up to 12 GPa. The melt T_g slightly decreases as pressure increases up to ~6-7 GPa, and then it significantly increases by ~31 % up to 12 GPa (Fig. 9). This behavior is similar to that observed for aluminium-rich albite $NaAlSi_3O_8$ melt by Bagdassarov et al. (2004). Those authors determined albite glass T_g up to ≈ 6 GPa via electrical impedance measurements during piston-cylinder and multianvil experiments. Their results show a decreasing albite glass T_g with increasing pressure up to ~6 GPa (Fig. 9). The ΔT_g versus pressure trend for albite glass exhibits a negative slope between 0 and 6 GPa, stronger than that for ANN glass (Fig. 9). Above ~6 GPa, there is no direct T_g data for albite melt but viscosity measurements give us further information (Kushiro, 1978; Funakoshi et al., 2002; Suzuki et al., 2002; Ashley et al., 2025): albite melt viscosity starts to increase with further increasing pressure.

This is coherent with the ANN T_g(P) evolution above 6 GPa (Fig. 9), which shows a positive slope similar to those of anorthite and peridotite melts (Fig. 9).

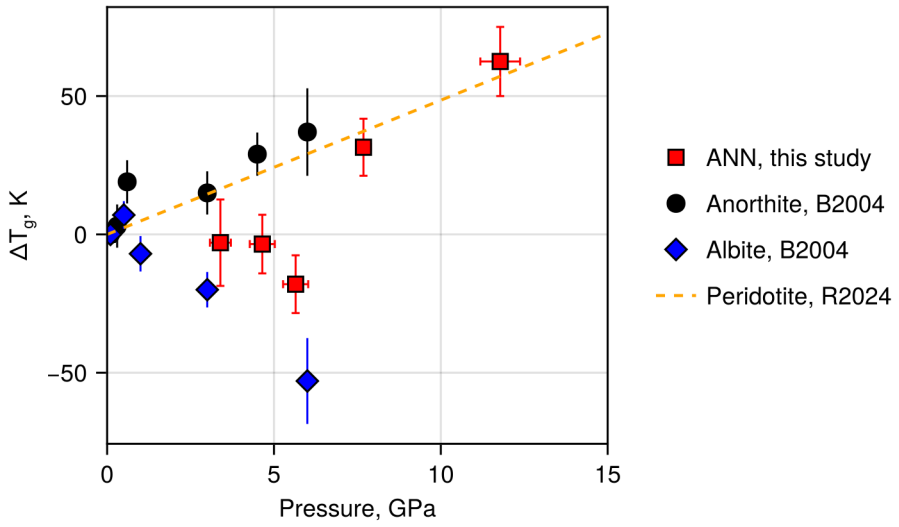

***Figure 9**: T_g values normalised to that at P = 1 atm, ΔT_g, represented as a function of pressure for ANN melt (this study), albite $NaAlSi_3O_8$ and anorthite $CaAl_2Si_2O_8$ melts (electrical impedance measurements, B2004: Bagdassarov et al., 2004), and peridotite melt (equation from R2024: Russell et al., 2024). For the present study, T_g values were set as the value between two glass/melt points during a run (see Fig. 6); their uncertainties are calculated combining the half-bracket width of the melt/glass interval with the measurement uncertainty on each bounding temperature.*

For alkali aluminosilicates (ANN and albite), the T_g(P) behaviour is consistent with different pressure response mechanisms below and above ~6-7 GPa. First, the initial decrease of T_g with increasing pressure (Fig. 9) is consistent with an initial compaction of the melt structure driven by a decrease in the T-O-T intertetrahedral angle, a collapse of the network free volumes, and possibly the conversion of some bridging oxygens to non-bridging oxygens due to volumetric effects (Bottinga and Richet, 1995; Wang et al., 2014; Ashley et al., 2025). For fully polymerized compositions such as albite, the BO→NBO conversion may be particularly effective (Bottinga and Richet, 1995; Wang et al., 2014). For the hydrous ANN melt (NBO/T ≈ 0.95), it is limited as shown by near constant Q^2/Q^3 ratio and Q^n Raman peak areas (Fig. 8). Instead, the pressure evolution of the mid-frequency Raman band centroid (Fig. 10) is consistent with network compaction dominated by decreasing T-O-T angles, as this band is sensitive to interpolyhedral angles (e.g., Weigel et al., 2016; Moulton et al., 2019). Notably, glasses and melts show shifted centroid values (Fig. 10), supporting the view that cold-compressed glasses and melts are not structurally equivalent over the investigated pressure range.

Then, at approximately 6–7 GPa, Raman data indicate a change in the dominant densification mechanism of the ANN melt. The mid-frequency Raman band shifts suddenly toward higher frequencies (Fig. 10), and the Q^2/Q^3 area ratio decreases (Fig. 8b). This

indicates an abrupt reorganisation of the polyhedral network above ~6-7 GPa, accompanied by increased melt polymerization, in agreement with previous Raman studies of high-pressure sodium silicate (Wolf et al., 1990a) and diopside (Moulton et al., 2016) glasses.

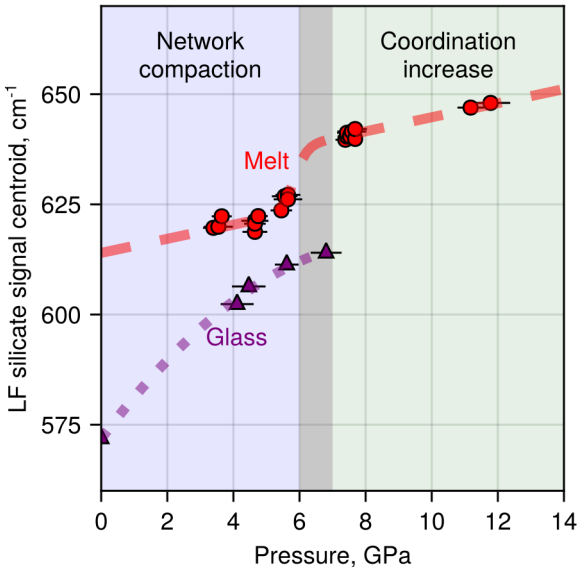

***Figure 10**: Centroid of the low-frequency Raman band (400-800 cm^{-1}) as a function of pressure, calculated from Raman spectra of cold-compressed glasses at 25 °C (triangles) and crystal-free undercooled melts above their T_g (circles) The blue and green shaded regions highlight two pressure regimes characterized by distinct evolutions of the low-frequency Raman centroid. The grey region marks the transition between these regimes, occurring near 6–7 GPa. The dashed and dotted thick lines are guides for the eyes.*

Taken together, these Raman observations are consistent with the onset of the transition of four-fold coordinated Si and Al, $^{[4]}$(Si,Al), toward six-fold coordinated $^{[6]}$(Si,Al) above the tetrahedral packing limit located at approximately 6-7 GPa (Wang et al., 2014), in agreement with previous experimental and simulation studies (e.g., Benmore et al., 2010; Wang et al., 2014; Lee et al., 2020). In the ANN melt, the coordination transition probably involves primarily Q^4 units because the increased polymerization does not result in more Q^4 units, as evidenced by a decreasing Q^4 peak area above ~6 GPa (Fig. 8a). In particular, as $^{[4]}$Al preferentially resides in Q^4 (e.g., Mysen et al., 2003; Le Losq et al., 2014), and as $^{[4]}$Al → $^{[6]}$Al occurs at lower pressures than $^{[4]}$Si → $^{[6]}$Si (Benmore et al., 2010; Yarger et al., 1995; Lee et al., 2020), we propose that the observed Raman variations reflect primarily the $^{[4]}$Al → $^{[6]}$Al transition. Of course, this does not exclude $^{[4]}$Si → $^{[6]}$Si, but we expect it to become dominant at higher pressures. This behaviour is consistent with previous observations on glasses quenched from high-pressure melts and analysed by nuclear magnetic resonance spectroscopy (Yarger et al., 1995; Allwardt et al., 2005). The joint increase in the T_{2s} peak area may then be explained assuming that signals from T-BO stretching mostly contribute to the T_{2s} peak (Mysen et al., 1982a). In this scenario, we hypothesize that T-BO stretching from polymerized $^{[5,6]}$(Si,Al) units contribute to the T_{2s} peak. To summarize, as pressure increases

above 6-7 GPa, the data on the ANN melt are consistent with the onset the $^{[4]}$(Si,Al) $\rightarrow^{[6]}$(Si,Al) transition, involving preferentially $^{[4]}$Al in Q^4 units, this resulting in increased T-O-T Raman signal frequencies (Fig. 10), decreased Q^2/Q^3 area ratio, higher T_{2s} peak area, lower Q^4 peak area (Fig. 8), and increased T_g (Figs. 6, 9).

Although this two-stage densification mechanism explains the pressure dependence of T_g in sodium aluminosilicate melts, other compositions exhibit different behaviors. For instance, both the fully polymerized anorthite as well as the depolymerized peridotite melts show a continuous, similar increase of their T_g (Fig. 9) and viscosity (Karki et al., 2011; Russell et al., 2024) with pressure. Similarly, alkaline-earth rich basalts with NBO/T around 0.7-1.0 show a continuous increase in viscosity with increasing pressure (Russell et al., 2025). It therefore seems that alkaline-earth-rich compositions exhibit a distinct pressure behavior.

The key to understanding these differences resides in the strong influence of melt composition on the medium-range organisation of the atomic network, which we propose as a determining factor driving the initial glass/melt pressure response. Indeed, compositions with identical polymerization but distinct medium range order organisation, such as albite and anorthite, show distinct T_g(P) behaviors (Fig. 9). This aligns with findings at one atmosphere: alkaline and calc-alkaline aluminosilicate melts presenting identical polymerization but distinct intermediate range order structure show very different thermodynamic and dynamic properties (e.g. Sreenivasan et al., 2020; Pannefieu et al., 2024). Even the simple exchange of one alkali (e.g. Na) by another (e.g. K) at constant polymerization induces an important re-organisation of the 2D/3D arrangements of tetrahedral units and of alkali cations in clusters and channels, driving important changes in aluminosilicate melt thermodynamic and dynamic properties (Le Losq and Neuville, 2013; Le Losq et al., 2017, 2021).

We therefore propose that the pressure response of silicate melts is governed by two successive structural regimes. Below the tetrahedral packing limit, the initial medium-range organisation of the melt structure controls the efficiency of network compaction because it determines the available free volume and the way tetrahedra can rearrange during the initial stages of compression. Therefore, depending on composition, we observe different pressure dependence of T_g. Above the tetrahedral packing limit, coordination changes become the dominant densification mechanism, and melts of widely differing compositions seem to converge toward a common positive T_g(P) behavior (Fig. 9) driven by the progressive formation of higher-coordinated network formers.

5. Conclusions

This study combined *in situ* Raman spectroscopy with high-temperature diamond anvil cell experiments to investigate the structural and dynamical evolution of a hydrous sodium aluminosilicate glass and undercooled melt up to 12 GPa. The disappearance of deviatoric stresses in the sample chamber provides a practical approach for estimating the glass transition temperature under high-pressure conditions, while Raman spectroscopy simultaneously probes the evolution of the melt structure. Together, these measurements

establish a new experimental framework for investigating the relationship between melt structure and dynamics at mantle pressures.

The Raman spectra reveal two distinct pressure regimes. Up to approximately 6 GPa, the melt structure undergoes progressive compaction, resulting in a slight decrease in T_g. At higher pressures, Raman spectra indicate increasing polymerization together with the onset of the 4 → 6 coordination transition, leading to a marked increase in T_g of about 30% between 6 and 12 GPa. These observations are consistent with a two-stage densification mechanism, in which the collapse of the existing network dominates at low pressure before coordination changes become the primary driver of structural evolution.

Our results also demonstrate that a glass compressed from ambient pressure is not structurally equivalent to a glass or melt equilibrated at the same pressure. Instead, the initial medium-range order inherited from the ambient-pressure structure exerts a strong control on the early stages of compression and on the associated changes in dynamical properties. Once coordination changes become the dominant densification mechanism, however, melts with markedly different chemical compositions exhibit remarkably similar positive T_g(P) slopes, suggesting that the high-pressure evolution of silicate melts may be governed by common structural processes.

Beyond the specific case of the ANN composition, this work demonstrates that simultaneous Raman spectroscopy and T_g determination provides a practical route toward experimentally constrained, structure-based models of silicate melt viscosity at high pressure. Extending this approach through combined Raman and Brillouin spectroscopy would provide simultaneous constraints on glass transition temperature, elastic properties and melt fragility (e.g., Cassetta et al., 2021). Applied to a broad range of silicate compositions, such measurements could establish the experimental foundation needed to develop predictive viscosity models for melts relevant to the deep interiors and magma oceans of rocky planets.

Funding

This study was supported by a Labex UnivEarthS grant, ANR-10-LABX0023 and ANR-18-IDEX-0001, and by a Chaire d'Excellence grant, ANR-18-IDEX-0001, to CLL.

Acknowledgements

We warmly thank Pierre Condamine (LMV University Clermont Auvergne) for discussions about piston-cylinder experiments, Stefan Klotz (IMPMC, Sorbonne University) for the SrB_4O_7:Sm^{2+} powder and discussions, Hélène Bureau (IMPMC, Sorbonne University), Yoann Guarnelli (IMPMC, Sorbonne University), Paraskevas Parisiadis (IMPMC, Sorbonne University), Bjorn Mysen (EPL, Carnegie Institution for Science), Dionysis Foustoukos (EPL, Carnegie Institution for Science) for discussions regarding diamond anvil cell experiments, and James Badro (IPGP) and Nicolas Wehr (IPGP) for their help and training at IPGP.

Declaration of Generative AI and AI-assisted technologies in the writing process.

We used ChatGPT (OpenAI) during the final preparation of this manuscript to review the English language and improve the clarity of the text. Prompts asked the model to identify grammatical, syntactic and stylistic issues, suggest improvements to readability and logical flow, and identify unnecessary repetition. Based on these suggestions, we made minor language edits, reduced repetition in the Results section, and improved the clarity and organisation of parts of the Discussion and Conclusions. All scientific interpretations, analyses, and final editorial decisions were made by the authors, who reviewed and approved all changes.

References

Allwardt, J.R., Stebbins, J.F., Schmidt, B.C., Frost, D.J., Withers, A.C., Hirschmann, M.M., 2005. Aluminum coordination and the densification of high-pressure aluminosilicate glasses. Am. Mineral. 90, 1218–1222. https://doi.org/10.2138/am.2005.1836

Ashley, A.W., Mookherjee, M., Xu, M., Yu, T., Manthilake, G., Wang, Y., 2025. The Viscosity of Albitic Melt at High Pressures and Implications for the Mobility of Crust-Forming Magmas. J. Geophys. Res. Solid Earth 130, e2024JB030527. https://doi.org/10.1029/2024JB030527

Bagdassarov, N.S., Maumus, J., Poe, B., Slutskiy, A.B., Bulatov, K., 2004. Pressure dependence of Tg in Silicate Glasses from Electrical Impedance Measurements. Phys. Chem. Glas.

Bajgain, S.K., Ashley, A.W., Mookherjee, M., Ghosh, D.B., Karki, B.B., 2022. Insights into magma ocean dynamics from the transport properties of basaltic melt. Nat. Commun. 13, 7590. https://doi.org/10.1038/s41467-022-35171-y

Bauchy, M., 2012. Structural, vibrational, and thermal properties of densified silicates: Insights from molecular dynamics. J. Chem. Phys. 137, 044510. https://doi.org/10.1063/1.4738501

Benmore, C.J., Soignard, E., Amin, S.A., Guthrie, M., Shastri, S.D., Lee, P.L., Yarger, J.L., 2010. Structural and topological changes in silica glass at pressure. Phys. Rev. B 81, 054105. https://doi.org/10.1103/PhysRevB.81.054105

Bottinga, Y., Richet, P., 1995. Silicate melts: The “anomalous” pressure dependence of the viscosity. Geochim. Cosmochim. Acta 59, 2725–2731. https://doi.org/10.1016/0016-7037(95)00168-Y

Brawer, S.A., White, W.B., 1977. Raman spectroscopic investigation of the structure of silicate glasses (II). Soda-alkaline earth-alumina ternary and quaternary glasses. J. Non-Cryst. Solids 23, 261–278. https://doi.org/10.1016/0022-3093(77)90009-6

Brawer, S.A., White, W.B., 1975. Raman spectroscopic investigation of the structure of silicate glasses. I. The binary alkali silicates. J. Chem. Phys. 63, 2421–2432. https://doi.org/10.1063/1.431671

Brooker, M.H., Nielsen, O.F., Praestgaard, E., 1988. Assessment of correction procedures for reduction of Raman spectra. J. Raman Spectrosc. 19, 71–78. https://doi.org/10.1002/jrs.1250190202

Caracas, R., 2024. The thermal equation of state of the magma Ocean. Earth Planet. Sci. Lett. 637, 118724. https://doi.org/10.1016/j.epsl.2024.118724

Cassetta, M., Di Genova, D., Zanatta, M., Boffa Ballaran, T., Kurnosov, A., Giarola, M., Mariotto, G., 2021. Estimating the viscosity of volcanic melts from the vibrational properties of their parental glasses. Sci. Rep. 11, 13072. https://doi.org/10.1038/s41598-021-92407-5

Cochain, B., Sanloup, C., Leroy, C., Kono, Y., 2017. Viscosity of mafic magmas at high pressures. Geophys. Res. Lett. 44, 2016GL071600. https://doi.org/10.1002/2016GL071600

Condamine, P., Tournier, S., Charlier, B., Médard, E., Triantafyllou, A., Dalou, C., Tissandier, L., Lequin, D., Cartier, C., Füri, E., Burnard, P.G., Demouchy, S., Marrocchi, Y., 2022. Influence of intensive parameters and assemblies on friction evolution during piston-cylinder experiments. Am. Mineral. 107, 1575–1581. https://doi.org/10.2138/am-2022-7958

Dalou, C., Le Losq, C., Mysen, B.O., 2015. In situ study of the fractionation of hydrogen isotopes between aluminosilicate melts and coexisting aqueous fluids at high pressure and high temperature – Implications for the δD in magmatic processes. Earth Planet. Sci. Lett. 426, 158–166. https://doi.org/10.1016/j.epsl.2015.06.032

Datchi, F., Dewaele, A., Loubeyre, P., Letoullec, R., Le Godec, Y., Canny, B., 2007. Optical pressure sensors for high-pressure–high-temperature studies in a diamond anvil cell. High Press. Res. 27, 447–463. https://doi.org/10.1080/08957950701659593

Deubener, J., Müller, R., Behrens, H., Heide, G., 2003. Water and the glass transition temperature of silicate melts. J. Non-Cryst. Solids 330, 268–273.

Doweidar, H., 1996. The density of alkali silicate glasses in relation to the microstructure. J. Non-Cryst. Solids 194, 155–162.

Drewitt, J.W.E., Jahn, S., Sanloup, C., de Grouchy, C., Garbarino, G., Hennet, L., 2015. Development of chemical and topological structure in aluminosilicate liquids and glasses at high pressure. J Phys Condens Matter 105103.

Elkins-Tanton, L.T., 2012. Magma Oceans in the Inner Solar System. Annu. Rev. Earth Planet. Sci. 40, 113–139. https://doi.org/10.1146/annurev-earth-042711-105503

Fleet, M.E., Henderson, G.S., 1997. Structure-composition relations and Raman spectroscopy of high-pressure sodium silicates. Phys. Chem. Miner. 24, 345–355. https://doi.org/10.1007/s002690050048

Funakoshi, K., Suzuki, A., Terasaki, H., 2002. *In situ* viscosity measurements of albite melt under high pressure. J. Phys. Condens. Matter 14, 11343–11347. https://doi.org/10.1088/0953-8984/14/44/479

Furukawa, T., Fox, K.E., White, W.B., 1981. Raman spectroscopic investigation of the structure of silicate glasses. III. Raman intensities and structural units in sodium silicate glasses. J. Chem. Phys. 75, 3226–3237. https://doi.org/10.1063/1.442472

Galeener, F.L., Sen, P.N., 1978. Theory of the first-order vibrational spectra of disordered solids. Phys. Rev. B 17, 1928–1933.

Greaves, G.N., Ngai, K.L., 1995. Reconciling ionic-transport properties with atomic structure in oxide glasses. Phys. Rev. B 52, 6358–6380. https://doi.org/10.1103/PhysRevB.52.6358

Greaves, G.N., Sen, S., 2007. Inorganic glasses, glass-forming liquids and amorphizing solids. Adv. Phys. 56, 1–166. https://doi.org/10.1080/00018730601147426

Hemley, R.J., Mao, H.K., Bell, P.M., Mysen, B.O., 1986. Raman Spectroscopy of SiO_2 Glass at High Pressure. Phys. Rev. Lett. 57, 747–750. https://doi.org/10.1103/PhysRevLett.57.747

Huang, D., Li, Y., Murakami, M., 2024. Low Viscosity of Peridotite Liquid: Implications for Magma Ocean Dynamics. Geophys. Res. Lett. 51, e2023GL107608. https://doi.org/10.1029/2023GL107608

Huang, D., Murakami, M., Brodholt, J., McCammon, C., Petitgirard, S., 2022. Structural evolution in a pyrolitic magma ocean under mantle conditions. Earth Planet. Sci. Lett. 584, 117473. https://doi.org/10.1016/j.epsl.2022.117473

Huang, D., Siebert, J., Badro, J., 2021. High pressure partitioning behavior of Mo and W and late sulfur delivery during Earth's core formation. Geochim. Cosmochim. Acta 310, 19–31. https://doi.org/10.1016/j.gca.2021.06.031

Hwang, H., Bang, Y., Choi, J., Cynn, H., Jenei, Z., Evans, W.J., Ehnes, A., Schwark, I., Glazyrin, K., Gatta, G.D., Lotti, P., Sanloup, C., Lee, Y., Liermann, H.-P., 2023. Graphite resistive heated diamond anvil cell for simultaneous high-pressure and high-temperature diffraction experiments. Rev. Sci. Instrum. 94, 083903. https://doi.org/10.1063/5.0132981

Karki, B.B., Bohara, B., Stixrude, L., 2011. First-principles study of diffusion and viscosity of anorthite (CaAl2Si2O8) liquid at high pressure. Am. Mineral. 96, 744–751.

Kolzenburg, S., Chevrel, M.O., Dingwell, D.B., 2022. Magma / Suspension Rheology. Rev. Mineral. Geochem. 87, 639–720. https://doi.org/10.2138/rmg.2022.87.14

Kushiro, I., 1978. Viscosity and structural changes of albite ($NaAlSi_3O_8$) melt at high pressures. Earth Planet. Sci. Lett. 41, 87–90.

Le Losq, C., 2018. Rampy: a Python library for processing spectroscopic (IR, Raman, XAS...) data. https://doi.org/10.5281/zenodo.1168730

Le Losq, C., 2016. Spectra.jl: a Julia package for processing spectroscopic data.

Le Losq, C., Baldoni, B., 2023. Machine learning modeling of the atomic structure and physical properties of alkali and alkaline-earth aluminosilicate glasses and melts. J. Non-Cryst. Solids 617, 122481. https://doi.org/10.1016/j.jnoncrysol.2023.122481

Le Losq, C., Cody, G.D., Mysen, B.O., 2015a. Complex IR spectra of OH^- groups in silicate glasses: Implications for the use of the 4500 cm^{-1} IR peak as a marker of OH^- groups concentration. Am. Mineral. 100, 945–950. https://doi.org/10.2138/am-2015-5076

Le Losq, C., Ferraina, C., Sossi, P.A., Boukaré, C.-E., 2025. A general machine learning model of aluminosilicate melt viscosity and its application to the surface properties of dry lava planets. Earth Planet. Sci. Lett. 656, 119287. https://doi.org/10.1016/j.epsl.2025.119287

Le Losq, C., Mysen, B.O., Cody, G.D., 2022. Water solution mechanism in calcium aluminosilicate glasses and melts: insights from in and ex situ Raman and ^{29}Si NMR spectroscopy. Comptes Rendus Géoscience 354, 1–27. https://doi.org/10.5802/crgeos.127

Le Losq, C., Mysen, B.O., Cody, G.D., 2015b. Water and magmas: insights about the water solution mechanisms in alkali silicate melts from infrared, Raman, and ^{29}Si solid-state NMR spectroscopies. Prog. Earth Planet. Sci. 2. https://doi.org/10.1186/s40645-015-0052-7

Le Losq, C., Neuville, D.R., 2017. Molecular structure, configurational entropy and viscosity of silicate melts: Link through the Adam and Gibbs theory of viscous flow. J. Non-Cryst. Solids 463, 175–188. https://doi.org/10.1016/j.jnoncrysol.2017.02.010

Le Losq, C., Neuville, D.R., 2013. Effect of the Na/K mixing on the structure and the rheology of tectosilicate silica-rich melts. Chem. Geol. 346, 57–71. https://doi.org/http://dx.doi.org/10.1016/j.chemgeo.2012.09.009

Le Losq, C., Neuville, D.R., Chen, W., Florian, P., Massiot, D., Zhou, Z., Greaves, G.N., 2017. Percolation channels: a universal idea to describe the atomic structure and dynamics of glasses and melts. Sci. Rep. 7, 16490. https://doi.org/10.1038/s41598-017-16741-3

Le Losq, C., Neuville, D.R., Florian, P., Henderson, G.S., Massiot, D., 2014. The role of Al^{3+} on rheology and structural changes of sodium silicate and aluminosilicate glasses and melts. Geochim. Cosmochim. Acta 126, 495–517. https://doi.org/10.1016/j.gca.2013.11.010

Le Losq, C., Valentine, A.P., Mysen, B.O., Neuville, D.R., 2021. Structure and properties of alkali aluminosilicate glasses and melts: Insights from deep learning. Geochim. Cosmochim. Acta 314, 27–54. https://doi.org/10.1016/j.gca.2021.08.023

Lee, S.K., Mun, K.Y., Kim, Y.-H., Lhee, J., Okuchi, T., Lin, J.-F., 2020. Degree of Permanent Densification in Oxide Glasses upon Extreme Compression up to 24 GPa at Room Temperature. J. Phys. Chem. Lett. 11, 2917–2924. https://doi.org/10.1021/acs.jpclett.0c00709

Mader, H.M., Llewellin, E.W., Mueller, S.P., 2013. The rheology of two-phase magmas: A review and analysis. J. Volcanol. Geotherm. Res. 257, 135–158. https://doi.org/10.1016/j.jvolgeores.2013.02.014

Malfait, W.J., 2009. The 4500 cm^{-1} infrared absorption band in hydrous aluminosilicate glasses is a combination band of the fundamental Si,Al-OH and O-H vibrations. Am. Mineral. 94, 849–852.

McMillan, P.F., 1984. Structural studies of silicate glasses and melts - Applications and limitations of Raman spectroscopy. Am. Mineral. 69, 622–644.

Moulton, B.J.A., Henderson, G.S., Fukui, H., Hiraoka, N., de Ligny, D., Sonneville, C., Kanzaki, M., 2016. *In situ* structural changes of amorphous diopside (CaMgSi2O6) up to 20 GPa: A Raman and O *K*-edge X-ray Raman spectroscopic study. Geochim. Cosmochim. Acta 178, 41–61. https://doi.org/10.1016/j.gca.2016.01.020

Moulton, B.J.A., Henderson, G.S., Martinet, C., Martinez, V., Sonneville, C., de Ligny, D., 2019. Structure—longitudinal sound velocity relationships in glassy anorthite (CaAl2Si2O8) up to 20 GPa: An *in situ* Raman and Brillouin spectroscopy study. Geochim. Cosmochim. Acta 261, 132–144. https://doi.org/10.1016/j.gca.2019.06.047

Muniz, R.F., de Ligny, D., Martinet, C., Sandrini, M., Medina, A.N., Rohling, J.H., Baesso, M.L., Lima, S.M., Andrade, L.H.C., Guyot, Y., 2016. In situ structural analysis of calcium aluminosilicate glasses under high pressure. J. Phys. Condens. Matter 28, 315402. https://doi.org/10.1088/0953-8984/28/31/315402

Mysen, B.O., 2007. The solution behavior of H_2O in peralkaline aluminosilicate melts at high pressure with implications for properties of hydrous melts. Geochim. Cosmochim. Acta 71, 1820–1834. https://doi.org/10.1016/j.gca.2007.01.007

Mysen, B.O., 1999. Structure and properties of magmatic liquids: From haplobasalt to haploandesite. Geochim. Cosmochim. Acta 63, 95–112.

Mysen, B.O., 1995. Experimental, in situ, high-temperature studies of properties and structure of silicate melts relevant to magmatic processes. Eur. J. Mineral. 7, 745–766.

Mysen, B.O., 1990. Role of Al in depolymerized, peralkaline aluminosilicate melts in the systems Li_2O-Al_2O_3-SiO_2, Na_2O-Al_2O_3-SiO_2, and K_2O-Al_2O_3-SiO_2. Am. Mineral. 75, 120–134.

Mysen, B.O., Finger, L.W., Virgo, D., Seifert, F.A., 1982a. Curve-fitting of Raman spectra of silicate glasses. Am. Mineral. 67, 686–695.

Mysen, B.O., Frantz, J.D., 1994. Silicate melts at magmatic temperatures: in-situ structure determination to 1651°C and effect of temperature and bulk composition on the mixing behavior of structural units. Contrib. Mineral. Petrol. 117, 1–14.

Mysen, B.O., Frantz, J.D., 1993. Structure of silicate melts at high temperature: In-situ measurements in the system BaO-SiO_2. Am. Mineral. 78, 699–709.

692 Mysen, B.O., Lucier, A., Cody, G.D., 2003. The structural behavior of Al^{3+} in peralkaline
693 melts and glasses in the system Na_2O-Al_2O_3-SiO_2. Am. Mineral. 88, 1668–1678.

694 Mysen, B.O., Virgo, D., Seifert, F.A., 1982b. The structure of silicate melts: Implications for
695 chemical and physical properties of natural magma. Rev. Geophys. 20, 353–383.
696 https://doi.org/10.1029/RG020i003p00353

697 Nesbitt, H.W., Henderson, G.S., Bancroft, G.M., Neuville, D.R., 2021. Spectral Resolution
698 and Raman Q^3 and Q^2 cross sections in ~40 mol% Na_2O glasses. Chem. Geol. 562,
699 120040. https://doi.org/10.1016/j.chemgeo.2020.120040

700 Nesbitt, H.W., O'Shaughnessy, C., Henderson, G.S., Michael Bancroft, G., Neuville, D.R.,
701 2019. Factors affecting line shapes and intensities of Q^3 and Q^4 Raman bands of Cs
702 silicate glasses. Chem. Geol. 505, 1–11.
703 https://doi.org/10.1016/j.chemgeo.2018.12.009

704 Neuville, D.R., 2006. Viscosity, structure and mixing in (Ca, Na) silicate melts. Chem. Geol.,
705 Physics, Chemistry and Rheology of Silicate Melts and Glasses 229, 28–41.
706 https://doi.org/10.1016/j.chemgeo.2006.01.008

707 Neuville, D.R., Cormier, L., Caurant, D., Montagne, L., 2017. From Glass to Crystal.
708 Nucleation, growth and phase separation: from research to applications. EDP
709 Sciences, France.

710 Neuville, D.R., Mysen, B.O., 1996. Role of aluminium in the silicate network: In situ,
711 high-temperature study of glasses and melts on the join SiO_2-$NaAlO_2$. Geochim.
712 Cosmochim. Acta 60, 1727–1737.

713 O'Shaughnessy, C., Henderson, G.S., Nesbitt, H.W., Bancroft, G.M., Neuville, D.R., 2020.
714 The influence of modifier cations on the Raman stretching modes of Qn species in
715 alkali silicate glasses. J. Am. Ceram. Soc. 103, 3991–4001.
716 https://doi.org/https://doi.org/10.1111/jace.17081

717 Pannefieu, S., Le Losq, C., Florian, P., Moretti, R., 2024. Effect of the Na/Mg mixing on the
718 structure and properties of aluminosilicate melts. J. Non-Cryst. Solids 637, 123056.
719 https://doi.org/10.1016/j.jnoncrysol.2024.123056

720 Piermarini, G.J., Block, S., Barnett, J.D., 1973. Hydrostatic limits in liquids and solids to 100
721 kbar. J. Appl. Phys. 44, 5377–5382. https://doi.org/10.1063/1.1662159

722 Ransom, T.C., Oliver, W.F., 2017. Glass Transition Temperature and Density Scaling in
723 Cumene at Very High Pressure. Phys. Rev. Lett. 119, 025702.
724 https://doi.org/10.1103/PhysRevLett.119.025702

725 Ribeiro, M.C.C., Pádua, A.A.H., Gomes, M.F.C., 2014a. Glass transition of ionic liquids
726 under high pressure. J. Chem. Phys. 140, 244514. https://doi.org/10.1063/1.4885361

727 Ribeiro, M.C.C., Pádua, A.A.H., Gomes, M.F.C., 2014b. Glass transition of ionic liquids
728 under high pressure. J. Chem. Phys. 140, 244514. https://doi.org/10.1063/1.4885361

Russell, J.K., Hess, K.-U., Anzulovic, A., Dingwell, D.B., 2025. Basalt melts under pressure: Is there really a viscosity minimum? Chem. Geol. 695, 123051. https://doi.org/10.1016/j.chemgeo.2025.123051

Russell, J.K., Hess, K.-U., Dingwell, D.B., 2024. Ultramafic melt viscosity: A model. Earth Planet. Sci. Lett. 643, 118899. https://doi.org/10.1016/j.epsl.2024.118899

Russell, J.K., Hess, K.-U., Dingwell, D.B., 2022. Models for Viscosity of Geological Melts. Rev. Mineral. Geochem. 87, 841–885. https://doi.org/10.2138/rmg.2022.87.18

Saha, P., Murakami, M., Sossi, P.A., Kitao, S., Seto, M., Mitsui, T., Lefebvre, P., Allaz, J., 2026. Ultrahigh-pressure acoustic velocities of ferric-iron-rich pyrolite glass: implications for ferric-rich silicate melts in the deep terrestrial interior. Earth Planet. Sci. Lett. 689, 120122. https://doi.org/10.1016/j.epsl.2026.120122

Sakamaki, T., Ohtani, E., 2022. High Pressure Melts. Rev. Mineral. Geochem. 87, 557–574. https://doi.org/10.2138/rmg.2022.87.11

Sanloup, C., 2016. Density of magmas at depth. Chem. Geol. 429, 51–59. https://doi.org/10.1016/j.chemgeo.2016.03.002

Schairer, J.F., Bowen, N.L., 1956. The system Na_2O-Al_2O_3-SiO_2. Am. J. Sci. 254, 129–195.

Shen, G., Wang, Y., Dewaele, A., Wu, C., Fratanduono, D.E., Eggert, J., Klotz, S., Dziubek, K.F., Loubeyre, P., Fat'yanov, O.V., Asimow, P.D., Mashimo, T., Wentzcovitch, R.M.M., other members of the IPPS task group, 2020. Toward an international practical pressure scale: A proposal for an IPPS ruby gauge (IPPS-Ruby2020). High Press. Res. 40, 299–314. https://doi.org/10.1080/08957959.2020.1791107

Shuker, R., Gammon, R.W., 1970. Raman-scattering selection-rule breaking and the density of states in amorphous materials. Phys. Rev. Lett. 25, 222.

Siebert, J., Corgne, A., Ryerson, F.J., 2011. Systematics of metal–silicate partitioning for many siderophile elements applied to Earth's core formation. Geochim. Cosmochim. Acta 75, 1451–1489. https://doi.org/10.1016/j.gca.2010.12.013

Silver, L.A., Ihinger, P.D., Stolper, E., 1990. The influence of bulk composition on the speciation of water in silicate glasses. Contrib. Mineral. Petrol. 104, 142–162. https://doi.org/10.1007/BF00306439

Solomatov, V., 2015. Magma Oceans and Primordial Mantle Differentiation, in: Treatise on Geophysics. Elsevier, pp. 81–104. https://doi.org/10.1016/B978-0-444-53802-4.00155-X

Spiekermann, G., Steele-MacInnis, M., Schmidt, C., Jahn, S., 2012. Vibrational mode frequencies of silica species in SiO_2-H_2O liquids and glasses from ab initio molecular dynamics. J. Chem. Phys. 136, 154501. https://doi.org/10.1063/1.3703667

Sreenivasan, H., Kinnunen, P., Adesanya, E., Patanen, M., Kantola, A.M., Telkki, V.-V., Huttula, M., Cao, W., Provis, J.L., Illikainen, M., 2020. Field Strength of

Network-Modifying Cation Dictates the Structure of (Na-Mg) Aluminosilicate Glasses. Front. Mater. 7, 267. https://doi.org/10.3389/fmats.2020.00267

Stolper, A., 1982. Water in silicate glasses: An infrared spectroscopic study. Contrib. Mineral. Petrol. 81, 1–17.

Suzuki, A., Ohtani, E., Funakoshi, K., Terasaki, H., Kubo, T., 2002. Viscosity of albite melt at high pressure and high temperature. Physic Chem. Miner. 29, 159–165.

Tarantola, A., 2005. Inverse problem theory and methods for model parameter estimation. Society for Industrial and Applied Mathematics, Philadelphia, PA.

Virgo, D., Mysen, B.O., Kushiro, I., 1980. Anionic constitution of 1-Atmosphere silicate melts: implications for the structure of igneous melts. Science 208, 1371–1373. https://doi.org/10.1126/science.208.4450.1371

Wang, Y., Sakamaki, T., Skinner, L.B., Jing, Z., Yu, T., Kono, Y., Park, C., Shen, G., Rivers, M.L., Sutton, S.R., 2014. Atomistic insight into viscosity and density of silicate melts under pressure. Nat. Commun. 5, 3241. https://doi.org/10.1038/ncomms4241

Weigel, C., Foret, M., Hehlen, B., Kint, M., Clément, S., Polian, A., Vacher, R., Rufflé, B., 2016. Polarized Raman spectroscopy of SiO_2 under rare-gas compression. Phys. Rev. B 93, 224303. https://doi.org/10.1103/PhysRevB.93.224303

Wolf, G.H., Durben, D.J., McMillan, P.F., 1990a. High-pressure Raman spectroscopic study of sodium tetrasilicate (Na2Si4O9) glass. J. Chem. Phys. 93, 2280–2288. https://doi.org/10.1063/1.459007

Wolf, G.H., Durben, D.J., McMillan, P.F., 1990b. High-pressure Raman spectroscopic study of sodium tetrasilicate (Na2Si4O9) glass. J. Chem. Phys. 93, 2280–2288. https://doi.org/10.1063/1.459007

Xie, L., Yoneda, A., Katsura, T., Andrault, D., Tange, Y., Higo, Y., 2021. Direct Viscosity Measurement of Peridotite Melt to Lower-Mantle Conditions: A Further Support for a Fractional Magma-Ocean Solidification at the Top of the Lower Mantle. Geophys. Res. Lett. 48, e2021GL094507. https://doi.org/10.1029/2021GL094507

Yamashita, S., Behrens, H., Schmidt, B.C., Dupree, R., 2008. Water speciation in sodium silicate glasses based on NIR and NMR spectroscopy. Chem. Geol. 256, 231–241.

Yarger, J.L., Smith, K.H., Nieman, R.A., Diefenbacher, J., Wolf, G.H., Poe, B.T., McMillan, P.F., 1995. Al Coordination Changes in High-Pressure Aluminosilicate Liquids. Science 270, 1964–1967. https://doi.org/10.1126/science.270.5244.1964

Supplementary Materials for the Manuscript

Structural and dynamical properties of hydrous magmatic liquids at high pressure: insights from Raman spectroscopy observations during diamond anvil cell experiments.

Lauréna Mourand[1], Clément Ferraina[1,2], Salomé Pannefieu[1], Cyril Aubaud[1], Charles Le Losq[1,3]

[1]Université Paris Cité, Institut de physique du globe de Paris, CNRS, Paris, France

[2]Université de Lorraine, CNRS, CRPG, F-54000 Nancy, France

[3]Institut Universitaire de France, Paris, France

11

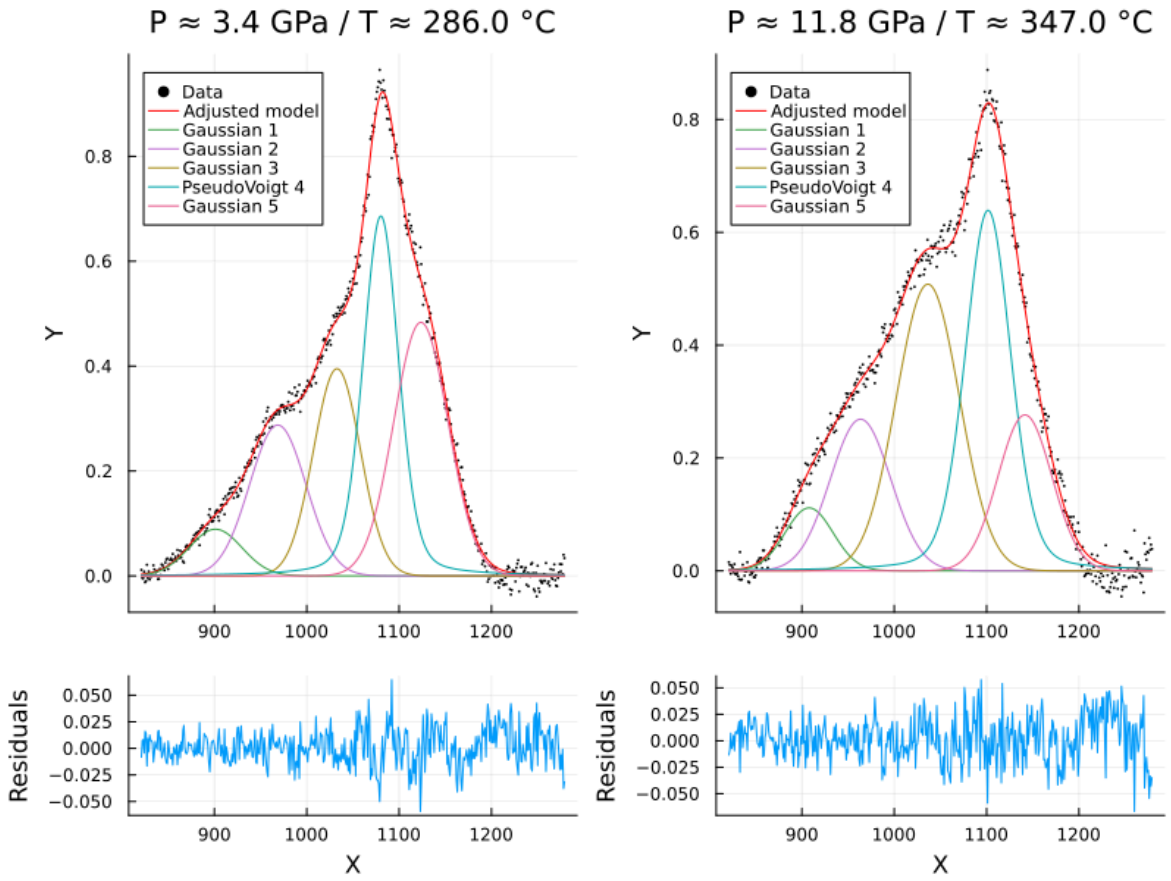

***Supplementary Figure 1**: Examples of peak fitting models of two Raman spectra acquired at around 3 and 12 GPa. Gaussian 1: TOH peak, Gaussian 2: Q^2 peak, Gaussian 3: T_{2S} peak, Pseudovoigt 4: Q^3 peak, and Gaussian 5: Q^4 peak. See main text for assignments.*

12

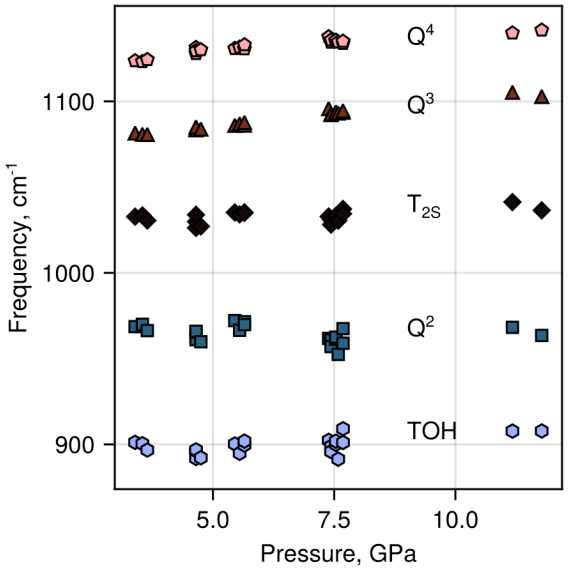

***Supplementary Figure 2**: Frequency of the peaks as a function of pressure, for Raman spectra acquired on melts.*

13

14

15

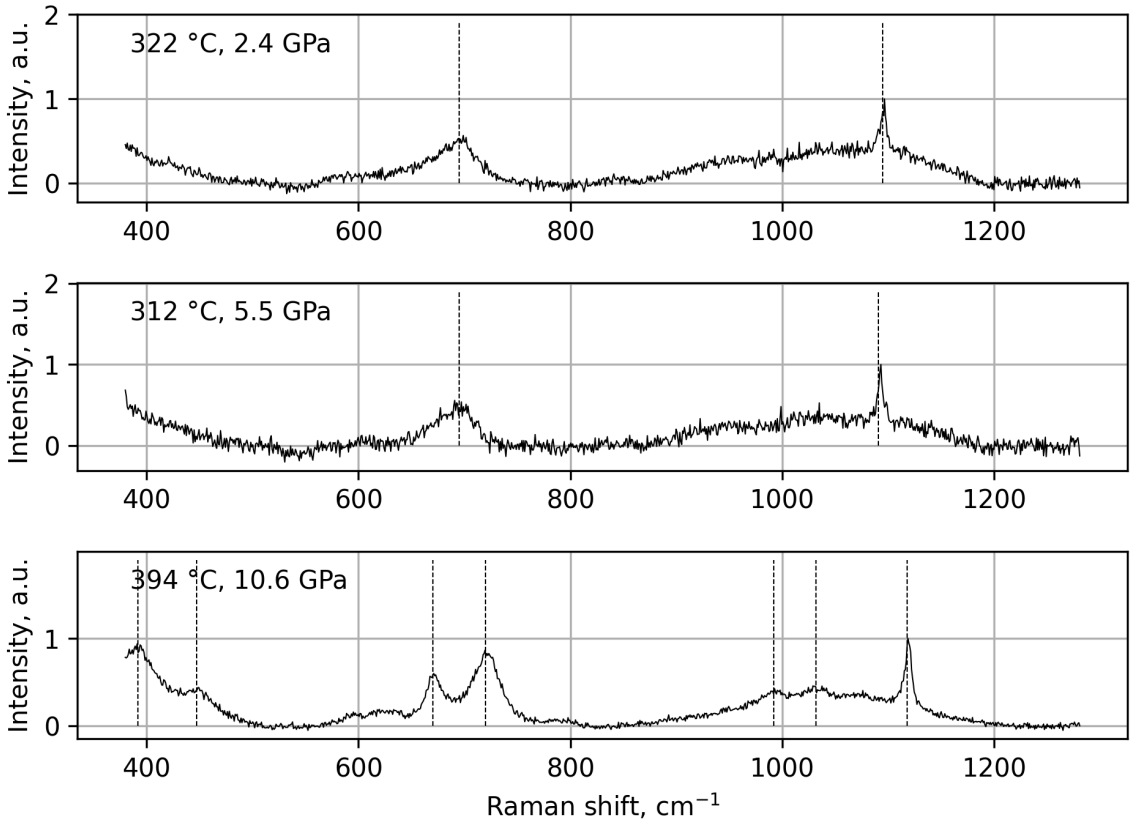

***Supplementary Figure 3**: Examples of Raman spectra acquired on the crystals that appeared in the MDAC sample chamber during three different runs, at different pressure/temperature conditions.*

16

17

18

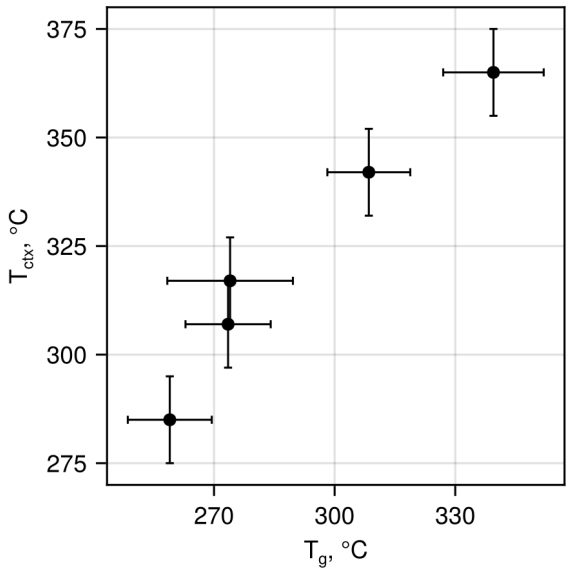

***Supplementary Figure 4**: Temperature at which crystallization was first visually observed (T_{CTX}, °C) represented as a function of the determined glass transition temperature (T_g, °C).*